Advances in Science and Technology Research Journal

Advances in Science and Technology Research Journal, 2026, 20(7), 263–277
https://doi.org/10.12913/22998624/219366
ISSN 2299-8624, License CC-BY 4.0

Received: 2026.01.05
Accepted: 2026.05.15
Published: 2026.06.01

Dynamic analysis of skew hollow-slab railway bridges under high-speed train loads using three-dimensional finite element and analytical beam models

Thang Ba Phung[1*], Dai Nguyen Xuan[2], Ly Kim Van[1], Khanh Nguyen[3]

[1] University of Transport Technology, Hanoi, Vietnam
[2] Le Quy Don Technical University, Hanoi, Vietnam
[3] Escuela Técnica Superior de Ingeniería Aeronáutica y del Espacio, UPM, Madrid, Spain
* Corresponding author's e-mail: thangpb@utt.edu.vn

ABSTRACT

On highway and railway lines, skew bridges are employed when the alignment intersects obstacles at non-orthogonal angles. The skew angle generates torsional moments in the bridge even when the applied loads are vertical and centrally positioned. In this study, an analytical method based on a simplified Euler–Bernoulli beam element model is used to perform the dynamic analysis of high-speed railway bridges, with particular attention to bridges with hollow-slab cross-sections subjected to high-speed Talgo 250 train loads. The influence of the skew angle is taken into account to determine the coupled flexo-torsional modes and subsequently dynamic vibrations. The analytical results are compared with those obtained from a three-dimensional finite element model (3D-FEM). Using the analytical approach, parametric studies are carried out to examine the effects of factors such as the skew angle, structural stiffness through the elastic modulus, and variations in cross-sectional shapes.

Keywords: skew bridges, hollow-slab bridges, three-dimensional finite element model, analytical beam model, dynamic analysis.

INTRODUCTION

In high-speed railway bridges, the dynamic impact effects of moving loads lead to an increase in internal forces, stresses, and deformations within the structure. When the natural frequencies of the bridge coincide with the excitation frequencies induced by the train loads, resonance phenomena may occur, resulting in a sudden amplification of bridge responses such as acceleration and deflection [1]. Excessive bridge accelerations adversely affect passenger comfort. According to European standards [2], in order to ensure passenger comfort, the allowable limit of bridge acceleration is 3.5 m/s² for bridges with ballasted tracks and 5.0 m/s² for bridges with slab track systems. Repeated dynamic responses of the bridge with high amplitudes may also lead to fatigue damage, cracking, and deterioration of the bridge structure as well as its connections and bearings. Therefore, in accordance with EN 1991-2, when train operating speeds are high, dynamic analysis must be performed to ensure the safe and smooth operation of trains [3].

A skew bridge structure is characterized by a non-zero angle between the line perpendicular to the longitudinal axis of the bridge and the centerline of the bearings. Under applied loads, the deck is subjected to coupled bending and torsional actions, leading to an asymmetric and more complex internal force distribution compared with that of straight bridges. Kollbrunner and Basler [4] were the first to describe the phenomenon of coupled bending–torsion behavior in skew beams and closed box sections and to introduce the concept of a skew-angle influence factor. Subsequent experimental investigations and numerical analyses have demonstrated the

significant effects of the skew angle on the natural frequencies, mode shapes, and internal force distribution of bridge superstructures [5–7].

In high-speed railway bridges, when the level of railway bridges in relation to the natural terrain is relatively low, simply supported bridges with short to medium spans of approximately 20–40 m commonly adopt hollow-slab cross-sections due to their high torsional stiffness and reasonable self-weight. Figure 1 illustrates a typical bridge cross-section with a width of 14 m, a structural depth of 1.76 m, and three longitudinal voids, designed for a double-track railway line [8]. In addition, this structural configuration offers the advantage of reducing the overall structural depth, thereby ensuring sufficient clearance beneath the bridge when crossing highways or other railway lines. In Spain, this type of structure is widely used, as exemplified by the Information Study Report on the Elche Urban Railway Network: Alignment option connecting the new High-Speed Railway Station with the urban center [9] as well as the Information Study Report on the Cantábrico–Mediterranean High-Speed Railway Corridor, section Zaragoza–Castejón [10].

The development of three-dimensional finite element models (full 3D FEM) has played a crucial role in elucidating the complex behavior of skew bridges, particularly the bending–torsion coupling and the asymmetric distribution of internal forces induced by skewed geometries, while also allowing the evaluation of local stresses and warping effects. Numerous experimental and numerical studies have demonstrated that only detailed 3D models can accurately capture stress variations, vibration modes, and the concentration of torsional moments at skewed bearings. He et al. [6] comprehensively validated a three-dimensional prestressed concrete box girder model through combined static and dynamic experiments, demonstrating significant discrepancies between the 3D model and simplified models as the skew angle increases. Another study by Kaliyaperumal et al. [11] on skew steel railway bridges showed that the combined effects of skew geometry and dynamic train loads lead to a substantial increase in edge torsion and vibration acceleration.

However, the full 3D FEM models require a large number of elements, long simulation times, and substantial computational resources, making them impractical for large-scale parametric studies. In contrast, a generalized beam element models with homogenized cross-sectional properties, employing beam theories such as Euler–Bernoulli or Timoshenko, allow for efficient and rapid analysis. For bridge structures with closed cross-sections, such as box girders or hollow slabs, the high torsional stiffness results in negligible warping deformations, making beam models sufficient to describe global dynamic behavior [12, 13]. To further reduce computational costs, refined Euler–Bernoulli beam models have been developed to reproduce the bending–torsion coupling of skew bridges. Meng and Lui employed stick models for skew bridges to perform dynamic analyses and to determine the natural frequencies and dominant mode shapes of the structures [14–16]. Ashebo et al. used analytical models to investigate the increase in dynamic load factors with skew angle in continuous box girder bridges [17]. Other classical studies, such as those by Maragakis–Jennings and Karnovsky, provide the theoretical foundation for displacement–torsion coupling modeling of skew beams [18, 19]. However, the majority of existing models focus on steel box girders or steel beams, while reinforced or prestressed concrete hollow-slab cross-sections have received limited attention.

For bridge structures with closed cross-sections, such as box girders or hollow slabs, the high torsional stiffness allows warping deformations to be neglected when the objective is to evaluate the global dynamic behavior. Accordingly, simplified beam models can be adopted, offering short modeling and analysis times while still ensuring satisfactory accuracy. Nguyen et al. (2019) investigated an analytical beam-modeling approach for a U-shaped girder for a single-track brigde subjected to centrally applied HSLMA1 train loads. The dynamic responses at the midspan were evaluated and compared with those obtained from stick-element and shell-element FEM models, showing differences of less than 5% [20].

This study investigates the applicability and performance of the analytical beam model proposed by Nguyen et al. [20] for a double-track hollow slab bridge, a structural system that exhibits a high degree of coupled bending–torsion behavior. A generalized, simplified analytical beam model is developed, and its predictions are evaluated against results obtained from a three-dimensional finite element model (3D FEM). The

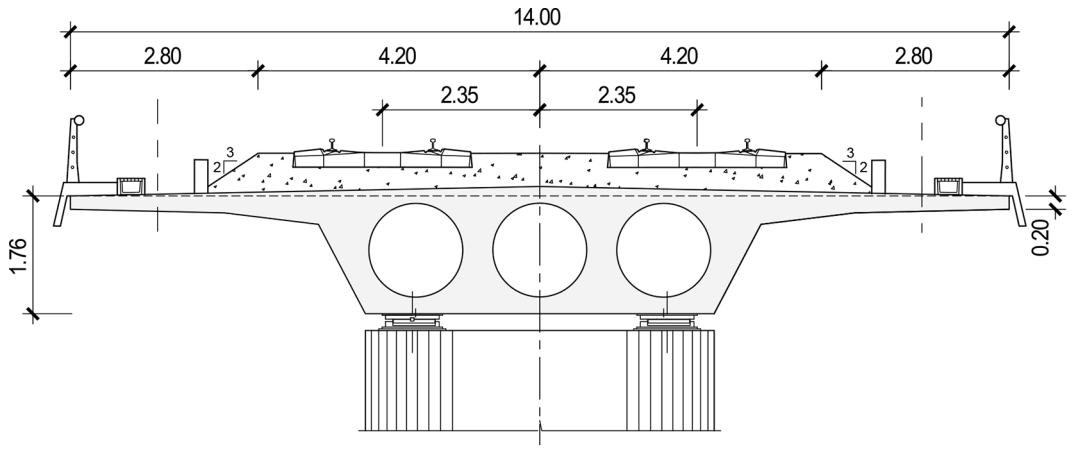

Figure 1. Typical cross-section of a hollow-slab bridge, adapted from [8]

resonance speeds predicted by both the analytical and numerical approaches are further compared with those specified in relevant design standards. Additionally, a parametric study is performed to examine the influence of skew angle, structural stiffness (represented by variations in Young's modulus), and cross-sectional configuration on the bridge's dynamic response.

GENERALIZED BEAM MODEL WITH TWO DEGREES OF FREEDOM

The generalized beam model is illustrated in Figure 2. The following assumptions are adopted:

1. A closed cross-section (such as a hollow slab or box girder) is considered; therefore, warping deformation and cross-sectional distortion are neglected, in accordance with the classical assumptions of Kollbrunner and Basler [4].
2. (The bridge girder is modeled as a linear elastic Euler–Bernoulli spatial beam, simply supported at both ends.
3. The in-plane stiffness in the horizontal xy plane is assumed to be sufficiently large; hence, lateral displacement is negligible and neglected.
4. The flexural stiffness *EI*, torsional stiffness *GJ*, and mass per unit length $\bar{m}$ are assumed to be uniform along the span length *L*.

Accordingly, the beam undergoes bending in the x−z plane and torsion about the longitudinal x-axis only. The governing differential equations of an Euler–Bernoulli beam in bending and Saint-Venant torsion can be expressed as [4,12,21]:

$$\bar{m}\ddot{u} + c_f\dot{u} + EI\frac{\partial^4 u}{\partial x^4} = p(x,t) \tag{1}$$

$$\bar{m}r^2\ddot{\theta} + c_t\dot{\theta} + GJ\frac{\partial^2 \theta}{\partial x^2} = m_t(x,t) \tag{2}$$

where: *r* is the radius of gyration, and $u(x,t)$ and $q(x,t)$ denote the vertical displacement and the torsional rotation of the bridge girder, respectively, which constitute two independent degrees of freedom (DOFs). The terms $p(x,t)$ and $m_t(x,t)$ represent the moving vertical load and the torsional moment, respectively, induced by skew effects or eccentric loading. The external damping components, $c_f\dot{u}$ and $c_t\dot{\theta}$ are assumed to be mass-proportional damping terms.

Using the method of separation of variables, the displacement field is expressed as a superposition of vibration modes:

$$\begin{Bmatrix} u(x,t) \\ \theta(x,t) \end{Bmatrix} = \sum_{n=1}^{\infty} q_n(t) \begin{Bmatrix} \phi_n(x,t) \\ \varphi_n(x,t) \end{Bmatrix} \tag{3}$$

where: $\phi_n(x,t)$ and correspond to the *n*th bending and torsional mode shapes, respectively, and, $q_n(t)$ denotes the generalized coordinate associated with the coupled bending–torsion response.

Substituting Equation 3 into Equations 1 and 2 yields the characteristic equation, and solving the resulting eigenvalue problem leads to two modal equations and the corresponding general solutions.

$$\begin{gathered} \phi_n(x) = C_{n,1}\,sin(\beta_n x) + \\ +C_{n,2}\,cos(\beta_n x) + C_{n,3}\,sinh(\beta_n x) \\ +C_{n,4}\,cosh(\beta_n x) \end{gathered} \tag{4}$$

$$\varphi_n(x) = C_{n,5}\, sin(\lambda_n x) + \\ +C_{n,6}\, cos(\lambda_n x) \tag{5}$$

where: $C_{n,i}$ (i=1-6) are constants determined from the boundary conditions; $\beta_n^4 = \frac{\bar{m}\omega_n^2}{EI}$, $\lambda_n^2 = \frac{\bar{m} r^2 \omega_n^2}{GJ}$.

From the boundary conditions of the skew bridge, including vertical displacement, rotations due to bending and torsion, and the bending–torsion moment relationships at both supports, an additional set of six boundary condition equations is obtained. Solving this system with the unknown constants $C_{n,i}$ yields the characteristic matrix A, whose determinant condition det(A)=0 leads to a nonlinear eigenvalue equation with respect to β. The solutions β_n (n = 1,2,3,…), determine the natural frequencies of the nth mode, as well as the associated constants and mode shapes. The resulting vibration modes must satisfy the orthogonality conditions.

To analyze the dynamic response of the bridge under moving loads, the mode superposition method is employed. For a concentrated load P, distributed loads, and torsional moments, the excitation terms can be expressed as:

$$P\delta(x - vt) \tag{6}$$

$$\ddot{q}_n(t) + 2\zeta\omega_n\dot{q}_n(t) + \omega_n^2 q_n(t) = Pa_n + \\ + \left[\frac{PL(\varepsilon - \varepsilon^2)\cot(\alpha)}{2(1 + K\cot^2(\alpha))} + Pe\right] b_n \tag{7}$$

where: $\delta(.)$ denotes the Dirac delta function, and $e = vt / L$, $K = EI / GJ$, e is the eccentricity of the applied load.

Using the mode superposition method together with the orthogonality conditions, the following uncoupled differential equations are obtained:

$$\ddot{q}_n(t) + 2\zeta\omega_n\dot{q}_n(t) + \omega_n^2 q_n(t) = Pa_n + \\ + \left[\frac{PL(\varepsilon - \varepsilon^2)\cot(\alpha)}{2(1 + K\cot^2(\alpha))} + Pe\right] b_n \tag{8}$$

where:

$$a_n = \phi_n(vt) \Big/ \left(\bar{m}\int_0^L \left[\phi_n(x)^2 + r^2\varphi_n(x)^2\right]dx\right)$$

$$b_n = \varphi_n(vt) \Big/ \left(\bar{m}\int_0^L \left[\phi_n(x)^2 + r^2\varphi_n(x)^2\right]dx\right)$$

denote the modal participation factors associated with the bending and torsional modes of order n, respectively.

Equation 8 is solved using the piecewise exact integration method [21] which is efficient for moving-load problems due to the exponential form of the solution in the time domain.

For a train load consisting of n_P axle loads, the modal equation corresponding to the n-th mode can be written as:

$$\ddot{q}_n(t) + 2\zeta\omega_n\dot{q}_n(t) + \omega_n^2 q_n(t) = \\ = \sum_{k=1}^{n_p}\left(P_k a_n + \left[\frac{PL(\varepsilon_k - \varepsilon_k^2)\cot(\alpha)}{2(1 + K\cot^2(\alpha))} + Pe\right] b_n\right) \\ \left[H\left(t - \frac{d_k}{v}\right) - H\left(t - \frac{d_k}{v} - \frac{L}{v}\right)\right] \tag{9}$$

where: n_P is the number of moving axle loads, d_k denotes the distance between the first axle load and the k-th axle load, and H(.) is the

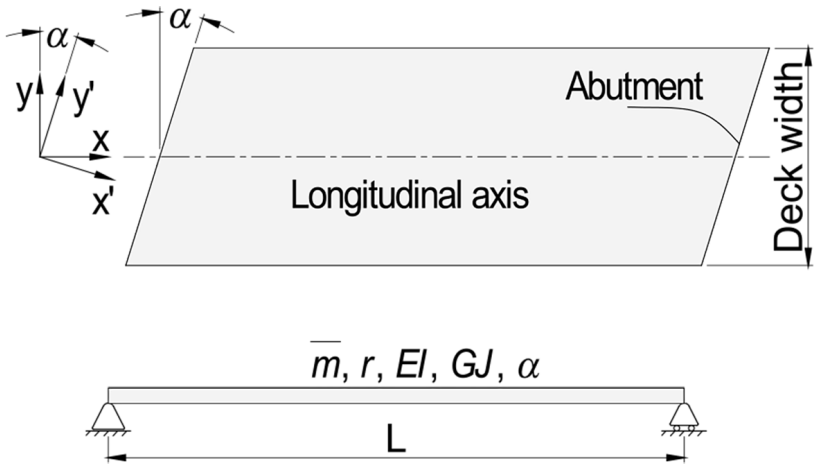

Figure 2. General model of the skew bridge, adapted from [20]

Heaviside step function used to determine whether a given axle load is acting on the bridge. If an axle has not yet entered the bridge or has already left it, its contribution is taken as zero.

NUMERICAL ANALYSIS OF SKEW HOLLOW-SLAB GIRDER BRIDGES

Case study

The structure considered in the analysis is a simply supported prestressed concrete hollow-slab bridge with a span length of L = 30 m and a skew angle of 30°. The bridge desk contains four longitudinal voids, with a deck width of B = 14 m, and a girder depth of h = 2.5 m. The detailed geometric dimensions are shown in the schematic illustration (Figure 3). In the present study, the prestressing tendons are not modeled explicitly, as the focus is on the global dynamic response of the bridge under moving train loads. The effect of prestressing is considered indirectly by assuming that the concrete section remains uncracked under service conditions, allowing the use of the corresponding elastic sectional stiffness in the dynamic analysis.

The geometric and material characteristics of the cross-section are summarized in Table 1.

The Talgo 250 high-speed train loads are applied along the track centerline, which is eccentrically located approximately 2.35 m from the bridge centerline. The axle loads and inter-axle spacings are summarized in Figure 4 and Table 2 [22].

Numerical analysis of a 3D model using the finite element method

The bridge structure is modelled using a three-dimensional finite element (3D FE) approach in Abaqus 6.14 [23], employing 8-node reduced-integration solid elements (C3D8R). A total of 80,799 elements are used, with an average element size of approximately 0.2 m.

For the dynamic analysis, the modal superposition method is adopted. The analysis considers the first 70 natural vibration modes. This large number of modes is required to identify the fundamental global vibration modes, as numerous local and coupled vibration modes are present due to the detailed 3D solid modeling. The first two flexural mode shapes occur at frequencies of f_1= 5.7018 Hz for mode 1 and f_2 = 21.9930Hz for mode 37, as illustrated in Figure 5.

Under the action of the actual Talgo 250 train loads, travelling at a speed of v = 250 km/h, the train runs along an eccentric track located 2.35 m away from the bridge centreline. The vertical displacement time histories in the y-direction at the midspan, evaluated at the cross-sectional centroid (Node 17) and at the track position (Node 18), are presented in Figure 6. The results indicate that the midspan displacement at the track location is governed not only by flexural behaviour, as observed at the cross-sectional centroid, but also by pronounced torsional effects induced by the eccentric loading. Consequently, the vertical displacement at the track location is consistently larger than that at the bridge centreline. Within the time interval from 0.25 s to 6.1 s, the displacement at the track location exceeds that at the cross-sectional centroid by a maximum of 22%, with an average increase of approximately 12% (Figure 6a). The vertical acceleration time histories in the y-direction at the midspan, evaluated at the bridge centreline (Node 17CDT) and at the track location (Node 18CDV, Track), are shown in Figure 6b.

Displacement and acceleration responses are obtained for train speeds ranging from 150 km/h to 350 km/h, with a speed increment of Δv = 5

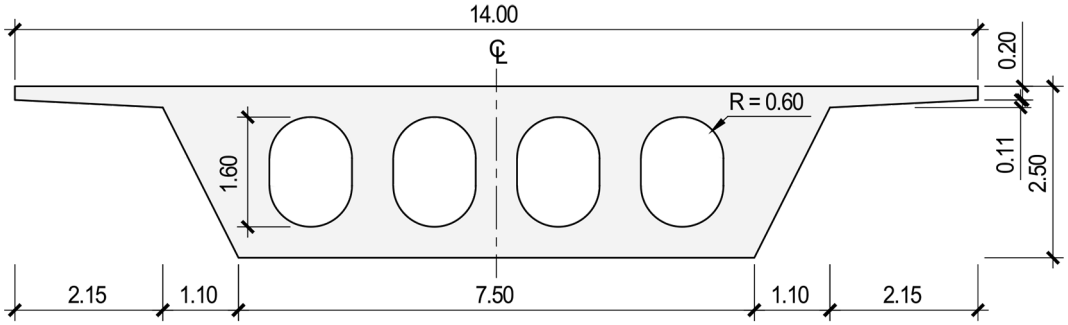

Figure 3. Cross-section of the hollow-slab girder

Table 1. Cross-sectional and material properties

Parameter	Symbol	Value	Unit
Cross-sectional area	A	16.5258	m^2
Bending moment of inertia	I	11.285098	m^4
Torsional constant	J	15.6420	m^4
Young's modulus	E	35	GPa
Shear modulus	G	14	GPa
Poisson's ratio	v	0.25	
Density	ρ	2500	kg/m^3
Structural damping ratio	ζ	0.02	

km/h. In the speed range from 270 km/h to 280 km/h, where resonance is likely to occur, a finer speed increment of 1 km/h is adopted. This analysis yields the envelope curves of the maximum displacement and acceleration responses at the midspan cross-section (L/2), evaluated at both the cross-section centreline and the railway track location, as shown in Figure 7. The envelope curves indicate that the peaks of both displacement and acceleration occur at a train speed of v = 276 km/h, which corresponds to the resonance speed of the bridge.

According to CEN (2023), the resonance speeds are calculated using the following formula:

$$v_i = f_0 \frac{D}{i}, \text{ with } i = 1, 2, 3,\ldots \tag{10}$$

The first flexural natural frequency obtained from the analysis is f_1 = 5.7018 Hz and the axle spacing of the train is D = 13.14 m, so the resonance speed is calculated as:

$$v = 3.6 \times 5.7018 \times 13.14/1 = 270 \text{ km/h}.$$

The discrepancy between the full three-dimensional finite element (3D FEM) model and the CEN-based analytical formula is relatively small: $\frac{276-270}{276} \approx 2\%$.

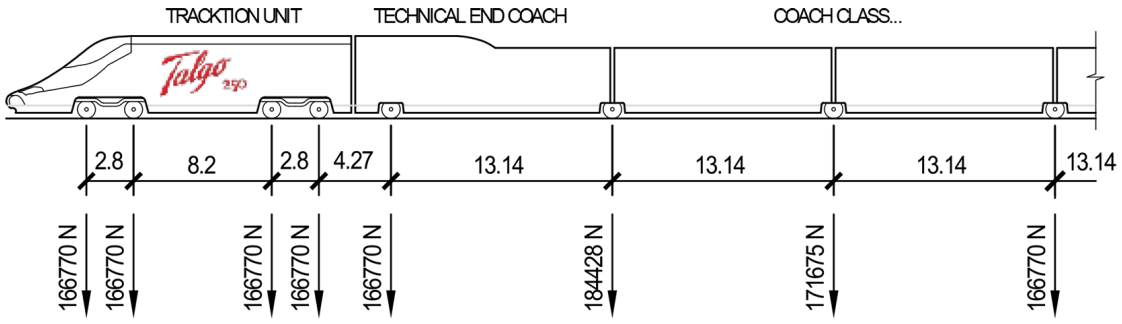

Figure 4. Talgo 250 configuration

Table 2. Axle spacing and loads of the Talgo 250 high-speed train

Axle spacing (m)	Axle load (N)	Axle spacing (m)	Axle load (N)	Axle spacing (m)	Axle load (N)
0	166770	13.14	173637	13.14	166770
2.8	166770	13.14	179523	13.14	173637
8.2	166770	13.14	166770	13.14	166770
2.8	166770	4.278	166770	13.14	173637
4.276	166770	2.8	166770	13.14	166770
13.14	184428	8.2	166770	13.14	173637
13.14	171675	2.8	166770	13.14	166770
13.14	166770	8.068	166770	13.14	173637
13.14	173637	2.8	166770	13.14	179523
13.14	166770	8.2	166770	13.14	166770
13.14	173637	2.8	166770	4.278	166770
13.14	166770	4.276	166770	2.8	166770
13.14	173637	13.14	184428	8.2	166770
13.14	166770	13.14	171675	2.8	166770

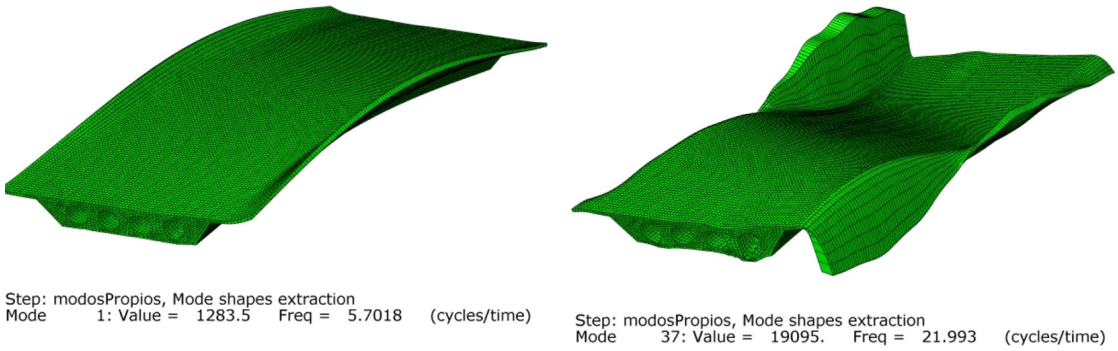

Figure 5. Three-dimensional finite element model and the first two flexural mode shapes

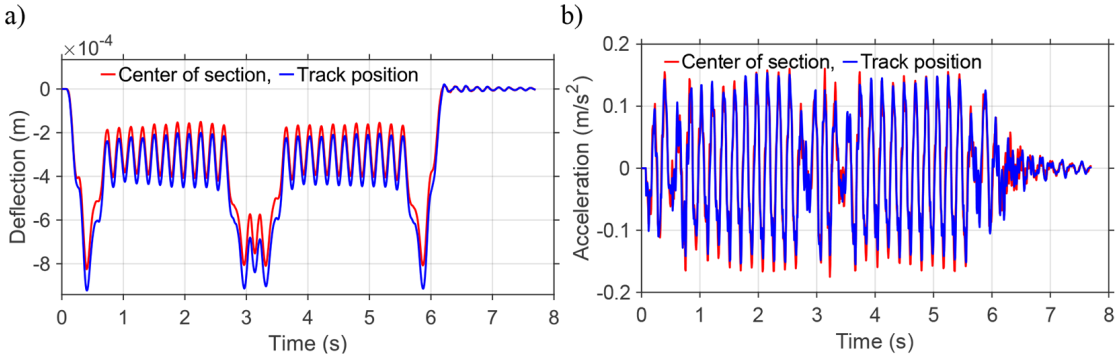

Figure 6. Vertical displacement (a) and acceleration (b) at the cross-section centreline and the track location at the midspan

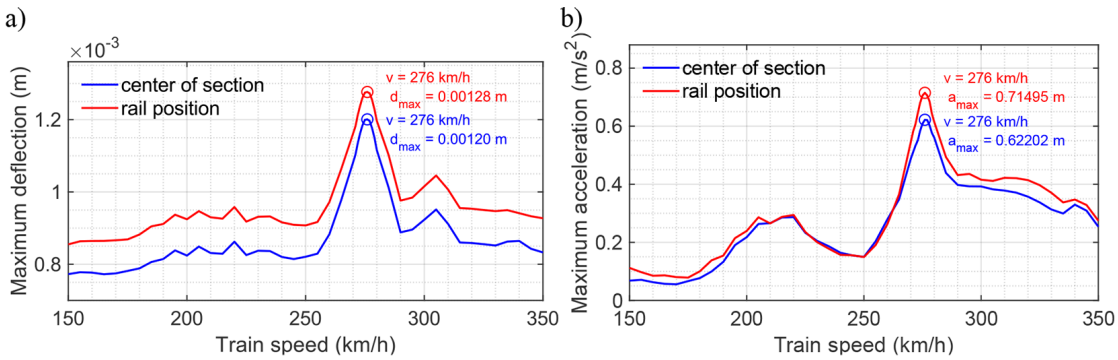

Figure 7. Envelope of the maximum deflection (a) and acceleration (b) induced by the Talgo 250 train loads at speeds ranging from 150 to 350 km/h

Figure 8 presents the displacement (a) and acceleration (b) responses at the resonance speed of v = 276 km/h. The results clearly demonstrate a pronounced amplification in both displacement and acceleration responses.

The three-dimensional finite element (3D FEM) model employed in this study offers the advantage of fully capturing the spatial structural behaviour of the bridge. It is capable of accounting for coupled flexural–torsional responses, modelling moving train loads, and performing modal analysis as well as time-domain dynamic analysis. Consequently, the model provides detailed results in terms of displacement and acceleration time histories, as well as envelope curves of maximum displacement and acceleration over a range of train speeds, which can be used to identify the resonance speed. However, the 3D FEM model is relatively complex and requires substantial effort in model development and computational time, particularly when a large number of train speeds must be considered or when parametric studies are carried out, such as investigations into the influence of the bridge skew angle.

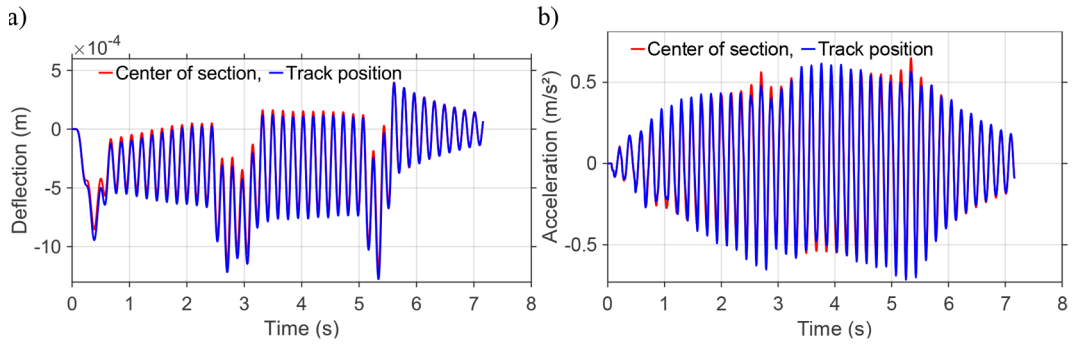

Figure 8. Displacement (a) and acceleration (b) induced by the Talgo 250 train loads at the resonance speed of v = 276 km/h

Analytical analysis based on a two-dimensional beam model

Using the analytical two-dimensional beam element model, a free-vibration analysis is performed to obtain the first three flexural modes, as summarized in Table 3. The differences between the 2D analytical model and the full three-dimensional finite element (3D FEM) model are relatively small, ranging from approximately 1% to 1.4%.

The time histories of bridge displacement and acceleration under the Talgo 250 train loads at a speed of v = 250 km/h are shown in Figure 9

For a bridge skew angle of 30°, the influence of train speed on the maximum displacement and maximum acceleration is investigated for speeds ranging from 150 km/h to 350 km/h, with a speed increment of 1 km/h. The results are presented in Figure 10. The peaks of the displacement and acceleration envelope curves occur at a train speed of v = 280 km/h, which corresponds to the resonance speed. Figure 11 illustrates the sudden amplification of displacement and acceleration responses at the resonance speed of v = 280 km/h.

The resonance speeds obtained using different approaches are summarized in Table 4.

The 3D FEM approach is regarded as a full and comprehensive model. The discrepancy between the 2D beam model and the 3D FEM model is approximately 1.4%, which can be attributed to the fact that the actual vibration behaviour of hollow-slab bridge structures involves significant transverse stiffness and torsional effects. In contrast, the CEN-based formula for calculating the resonance speed is formulated for flexural beam models that do not account for torsional modes. This observation differs from the findings reported by Nguyen et al [20] for U-girder bridges, where larger discrepancies were observed between the 3D FEM results, the CEN predictions, and the corresponding 2D beam models.

Table 3. Natural frequencies

Frequency	FEM 3D (Hz)	2D model (Hz)	Difference (%)
f_1	5.7018	5.7836	1.4
f_2	21.9930	21.7810	1.0
f_3	-	49.296	-

PARAMETRIC ANALYSIS

In this section, three parametric studies are performed using the analytical beam model in order to determine its influence on the dynamic responses of skew bridge.

Influence of the skew angle

The skew angle varies from 0° to 45° with increment of 5°. The bridge's properties are the same used in the previuos section.

The influence of the skew angle on the natural frequencies of the first three modes is presented in Table 5 and Figure 12. Based on the results, it can be observed that as the skew angle increases, the natural frequencies of the first and third modes increase more significantly than that of the second flexural mode. Specifically, as the skew angle increases from 0° to 45°, the first-mode natural frequency increases by $\frac{6.4182-5.4018}{5.4018}=19\%$, while the second and third modes increase by $\frac{22.1275-21.6071}{21.6071}=2\%$ and $\frac{50.5504-48.6160}{48.6160}=4\%$, respectively.

The maximum displacement and acceleration at midspan in function of train speed are illustrated by the two plots shown in Figure 13a, b. It is observed that the resonance speed increases with

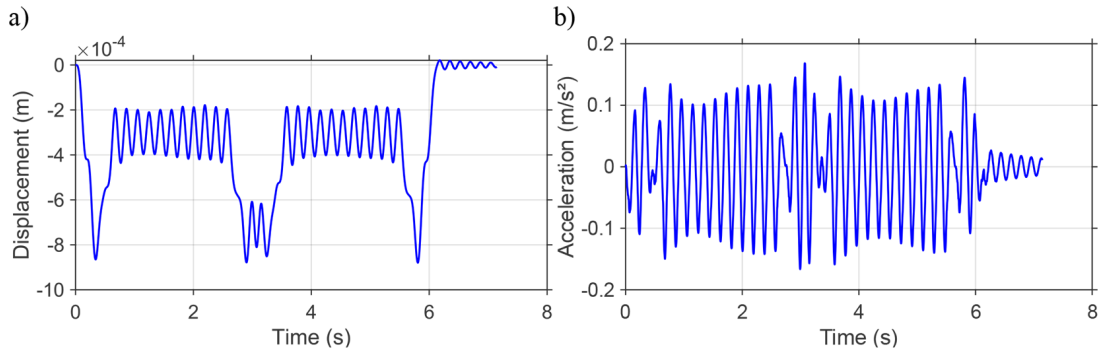

Figure 9. Displacement (a) and acceleration (b) responses at a train speed of v = 250 km/h

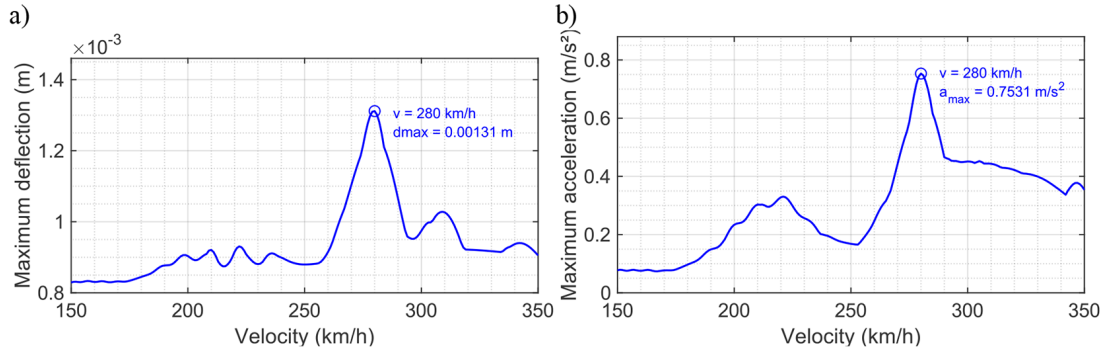

Figure 10. Relationship between train speed and maximum displacement (a) and maximum acceleration (b)

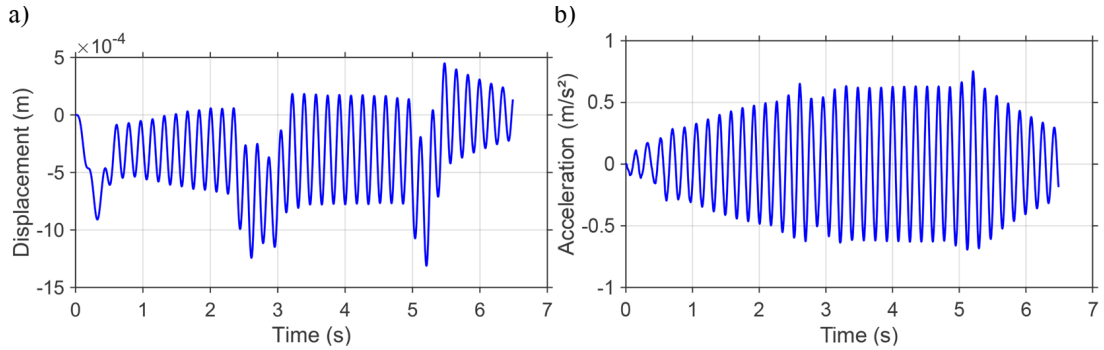

Figure 11. Displacement and acceleration responses at the resonance speed of v = 280 km/h

increasing skew angle, as expected, since the fundamental natural frequency also increases with the skew angle. This increase exhibits a nonlinear trend (Figure 13c): the more skewed the bridge, the higher the speed required to induce resonance. In other words, the skew effect shifts the resonance to higher train speeds.

The influence of the skew angle on the maximum displacement and acceleration is illustrated in Figures 14a, 14b. The results show that as the bridge skew angle increases, the maximum displacement decreases in a nonlinear manner, with a more pronounced reduction at larger skew angles (Figure 14a). By comparison, the maximum acceleration also decreases with increasing skew angle, but the variation is relatively small (Figure 14b).

This behaviour can be explained by the fact that the peak acceleration depends on both the vibration amplitude and the natural frequency, i.e., $a_{max} = \omega^2 d_{max}$. As the skew angle increases, the displacement amplitude decreases, while the natural frequency increases, leading to a limited overall change in the maximum acceleration.

Table 4. Resonance speeds by different methods

Parameter	FEM 3D	CEN	2D model	CEN
f_1 (Hz)	5.7018	5.7018	5.7836	5.7836
v (km/h)	276	270	280	274

Table 5. Influence of skew angle on first three vibration modes

Skew angle (°)	f_1 (Hz)	f_2 (Hz)	f_3 (Hz)
0	5.4018	21.6071	48.6160
5	5.4111	21.6111	48.6320
10	5.4397	21.6233	48.6810
15	5.4885	21.6446	48.7657
20	5.5598	21.6763	48.8909
25	5.6566	21.7206	49.0642
30	5.7836	21.7810	49.2967
35	5.9468	21.8628	49.6045
40	6.1546	21.9740	50.0111
45	6.4182	22.1275	50.5504

Influence of material properties

Among the material properties, the influence of the elastic modulus of concrete is investigated. The elastic modulus is varied from E=30 GPa to 50 GPa with an increment of 5 GPa, while the train speed ranges from 200 km/h to 400 km/h with a speed increment of 1 km/h. The relationships between train speed and the corresponding maximum displacement and maximum acceleration for different values of the concrete elastic modulus are illustrated in Figures 15a and 15b for a skew angle of 30°. In principle, an increase in the elastic modulus leads to an increase in bridge stiffness, which in turn results in higher natural frequencies and, consequently, higher critical/resonance speeds. This trend is clearly observed in the two plots. The figures also show that as E increases, the maximum displacement decreases (Figure 15a), whereas the maximum acceleration remains nearly unchanged (Figure 15b).

The relationships between train speed and the maximum displacement and acceleration are further investigated by simultaneously varying the elastic modulus of concrete (from 30 GPa to 50 GPa) and the skew angle (from 0° to 45°). The corresponding results are presented in Figures 16a and 16b. For each skew angle, a consistent trend can be observed: the resonance speed increases with increasing elastic modulus, and likewise, the resonance speed also increases as the skew angle becomes larger. As either the skew angle or the elastic modulus increases, the maximum displacement decreases (Figure 16a), while the maximum acceleration also shows a slight reduction, with only minor variations (Figure 16b).

Influence of cross-sectional geometry

To investigate the influence of void ratio in designing the hollow slab section, fifteen

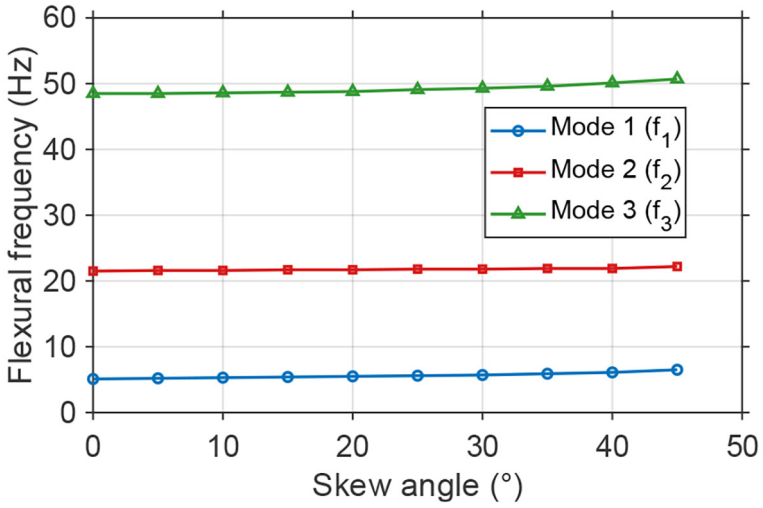

Figure 12. Influence of skew angle on first three flexural modes

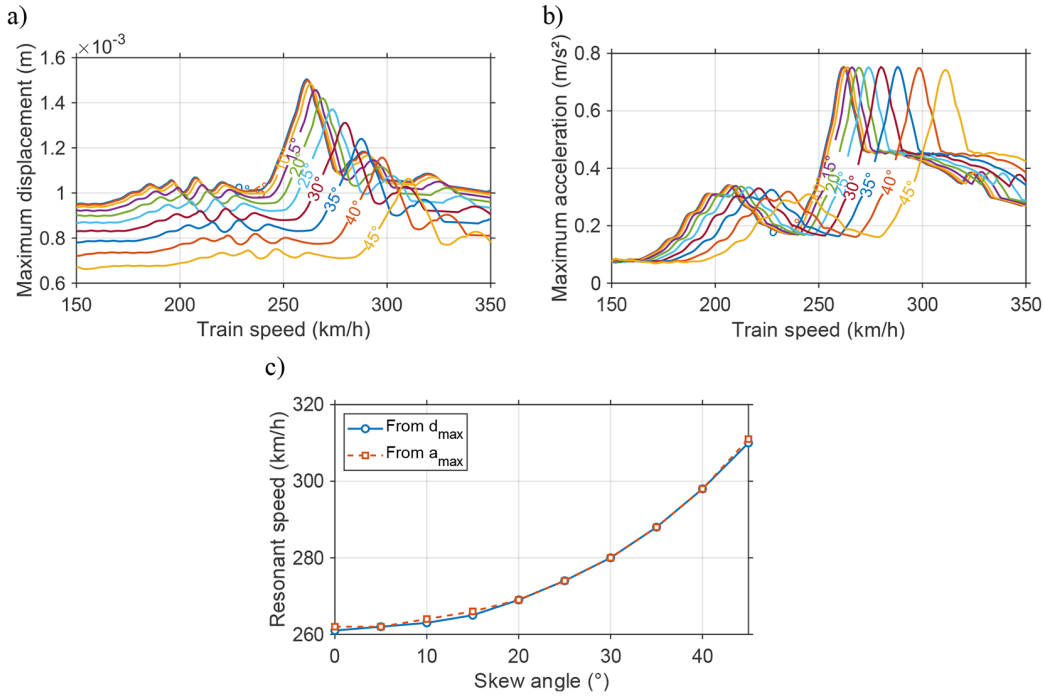

Figure 13. Influence of the skew angle on the resonance speed

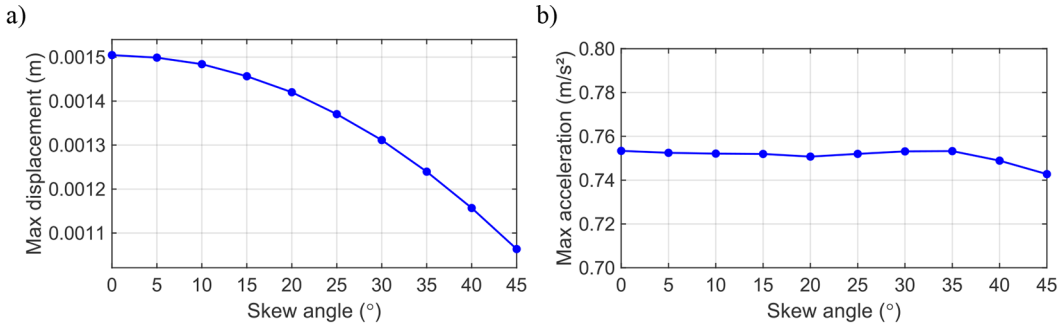

Figure 14. Influence of the skew angle on the maximum displacement and acceleration

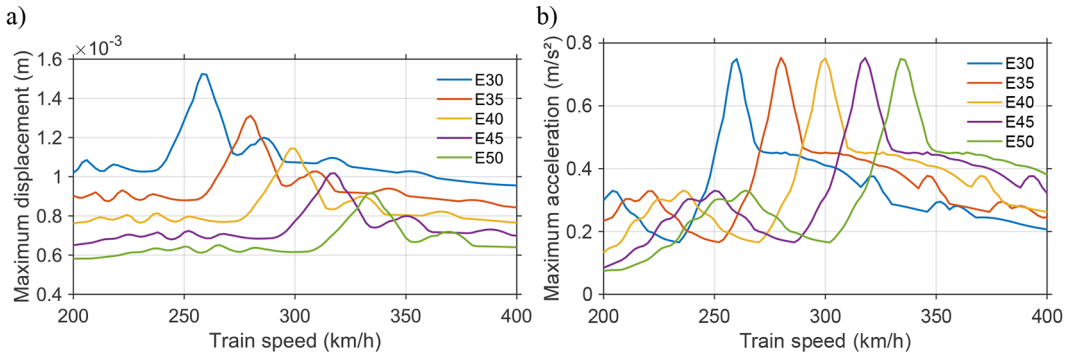

Figure 15. Speed–response relationships of maximum displacement and acceleration for different concrete elastic moduli at a skew angle of 30°

cross-sections with identical beam height and width but varying numbers and diameters of voids are considered, as illustrated in Figure 17. The cross-sections are classified into three groups, corresponding to sections with four voids, three voids, and two voids. The 2D analytical model is developed based on the Euler-Bernoulli beam theory, where the longitudinal voids are accounted

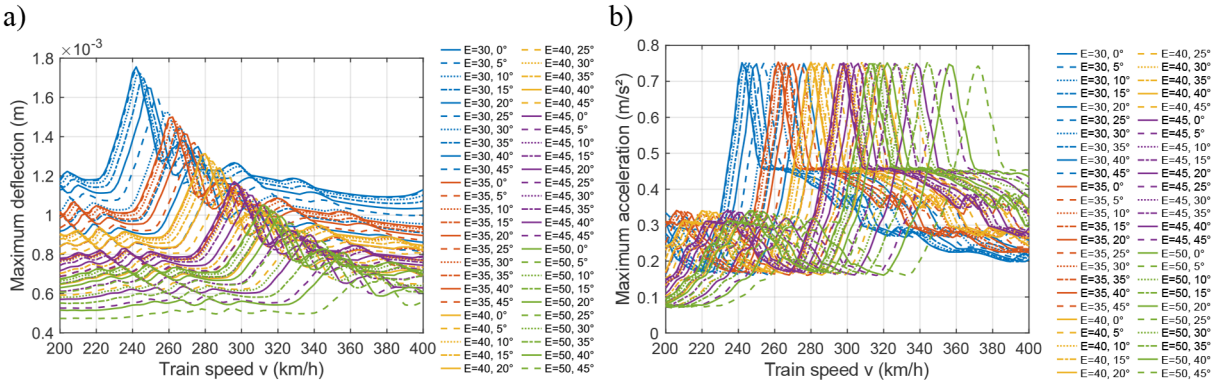

Figure 16. Train speed–response relationships for varying elastic moduli (E) and skew angles (α): (a) maximum displacement; (b) maximum acceleration

for using equivalent geometric properties (A, I, J, r) derived from the hollow cross-sections. These parameters for all investigated cases are detailed in Table 6, while the material properties remain consistent with the cases presented in Table 1. The parameters varied in the numerical model include the geometric properties and the mass of the beam. The bridge skew angle is fixed at 30° in this analysis.

A dynamic analysis of the bridge is performed under the action of Talgo 250 train loads travelling at speeds ranging from 150 km/h to 350 km/h, with a speed increment of 1 km/h. The resulting relationships between train speed and the corresponding maximum displacement and maximum acceleration are presented in Figures 18a and 18b. From the peaks of the speed–maximum displacement and speed–maximum acceleration curves, the resonance speeds for different cross-sectional configurations are identified and summarized in the bar chart shown in Figure 19.

The results indicate the same tendency of decreasing critical speed for all three groups as the void ratio decreases. Within each group, a reduction in void diameter leads to an increase in geometric properties; however, the associated increase in mass results in a decrease in the resonance speed.

The numerical results indicate that, for the same void diameter, Group 1 exhibits higher resonant speeds than Group 2, while Group 2 shows higher resonant speeds than Group 3. Specifically, for a void diameter of 1.6 m, the void areas of cross-sections S2, S7, and S12 are 8.04 m², 6.03 m², and 4.02 m², respectively, while the corresponding geometric properties, expressed by the second moment of area (I), are 11.04 m⁴, 11.40 m⁴, and 11.76 m⁴. As the void area decreases, considering only the increase in structural mass leads to a reduction in the resonant speed, whereas considering only the variation in geometric stiffness results in an increase in the resonant speed.

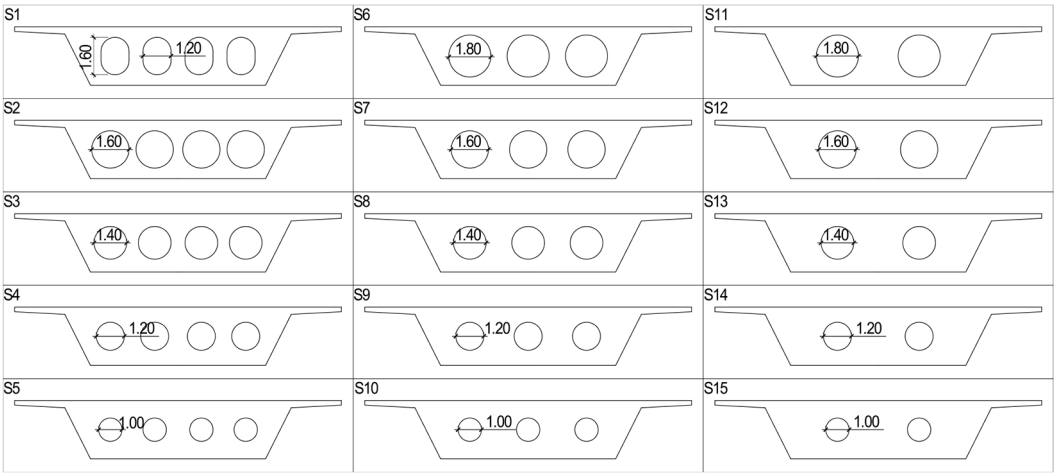

Figure 17. Different cross-sectional geometries (dimensions in m)

Table 6. Geometric properties of the cross-sections

Section	A (m²)	I (m⁴)	J (m⁴)	r (m)	Number of voids	Void geometry	Void diameter (m)
S1	16.52584	11.28510	31.28404	0.82636	4	rounded-rectangular	1.60
S2	14.94930	11.03881	30.41651	0.85931	4	circular	1.60
S3	16.82153	11.60999	32.73531	0.83077	4	circular	1.40
S4	18.44414	11.98467	34.37649	0.80609	4	circular	1.20
S5	19.81711	12.21576	35.45370	0.78513	4	circular	1.00
S6	15.35495	10.79407	29.21958	0.83843	3	circular	1.80
S7	16.94635	11.40472	31.93599	0.82036	3	circular	1.60
S8	18.35053	11.82652	33.81711	0.80279	3	circular	1.40
S9	19.56748	12.10425	35.08179	0.78651	3	circular	1.20
S10	20.59721	12.27595	35.91627	0.77201	3	circular	1.00
S11	17.88247	11.35911	31.18556	0.79700	2	circular	1.80
S12	18.94340	11.76039	33.26142	0.78792	2	circular	1.60
S13	19.87952	12.03837	34.75337	0.77818	2	circular	1.40
S14	20.69082	12.22175	35.69194	0.76856	2	circular	1.20
S15	21.37731	12.33529	36.24285	0.75962	2	circular	1.00

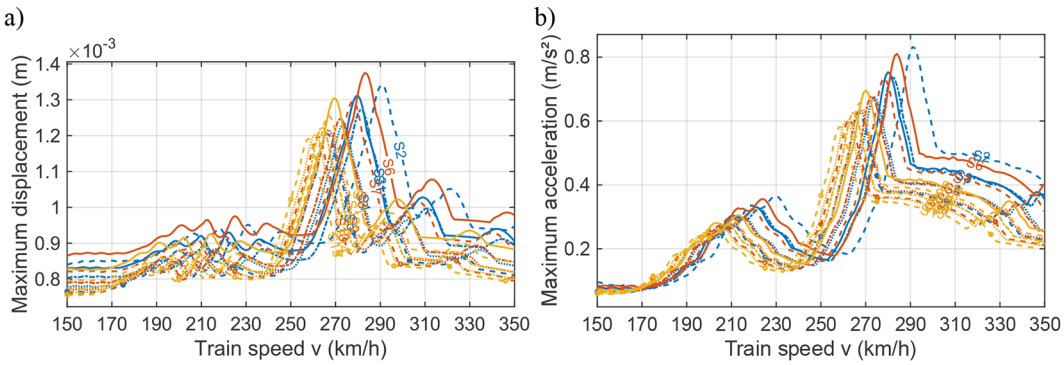

Figure 18. Relationship between train speed and structural responses for the 15 cross-sectional configurations: (a) displacement; (b) acceleration

When both effects are simultaneously taken into account, the resonant speed decreases, with corresponding values of 291 km/h, 278 km/h, and 267 km/h, respectively (Table 6 and Figure 19).

Within each group, a reduction in void diameter increases the geometric stiffness of the cross-section, which tends to increase the resonant speed. Conversely, the associated increase in structural mass leads to a reduction in the resonant speed. The dynamic analysis demonstrates that the mass effect dominates the structural dynamic response, resulting in an overall decrease in the resonant speed. In Group 2, the void area decreases from 7.63 m² to 2.35 m² (a reduction of 69%). Due to the counteracting effects of stiffness enhancement and mass increase, the resonant speed decreases from 284 km/h to 263 km/h, corresponding to a reduction of 7%. A similar trend is observed in Group 3, where a 69% reduction in void area results in a 4% decrease in the resonant speed. Group 1 exhibits the same tendency.

However, a different behavior is observed when comparing cross-sections S1 and S2. Cross-section S1 employs a rounded-rectangular void, leading to a smaller void area than that of S2 and, consequently, a larger structural mass. Although cross-section S1 exhibits greater geometric stiffness than S2, the mass effect governs the dynamic behavior of the HSR bridge. As a result, the resonant speed of the bridge with cross-section S1 is 280 km/h, which is lower than that of the bridge with cross-section S2 (291 km/h) (Table 6 and Figure 19).

Overall, the results indicate that the introduction of voids in HSR bridge cross-sections generally increases the resonant speed, primarily due to the governing influence of structural mass reduction.

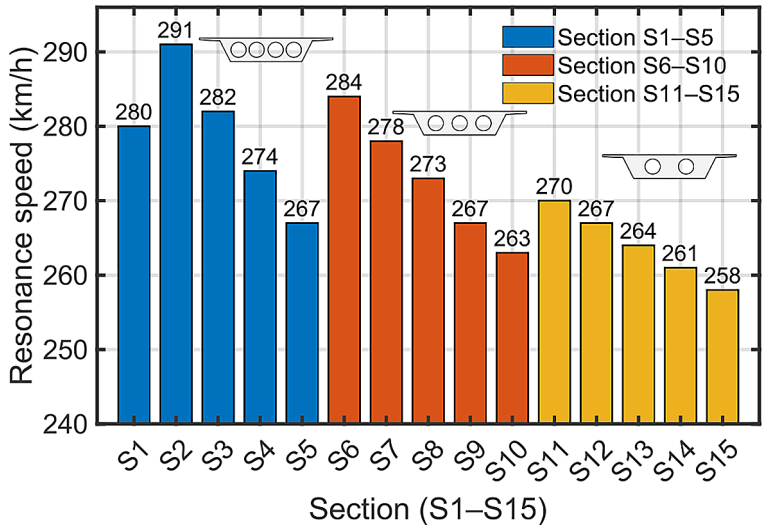

Figure 19. Resonance speeds for different cross-sectional configurations

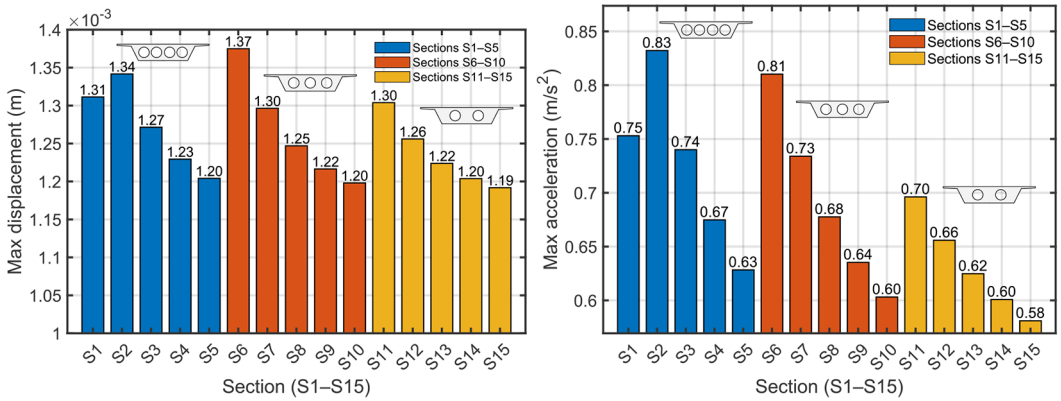

Figure 20. Maximum displacement for different cross-sectional configurations

Nevertheless, the selection of the number and diameter of voids must also consider structural detailing requirements and construction constraints.

The results for the maximum displacement and maximum acceleration exhibit trends similar to those observed for the resonance speed, as shown in Figure 20.

CONCLUSIONS

This study employed a three-dimensional finite element (3D FEM) model together with the development and application of a two-dimensional analytical beam model to investigate skew hollow-slab railway bridges subjected to eccentric loading from the actual Talgo 250 high-speed train. Based on the dynamic analyses of the bridge under free-vibration conditions and moving train loads, the following conclusions can be drawn:

5. The three-dimensional finite element model captures both flexural and torsional vibration modes of the skew hollow-slab bridge. The dynamic responses at the bridge centreline and at the eccentric track location differ significantly, with displacement differences averaging 12% and reaching up to 22%. The resonance speed under Talgo 250 train loading is identified as approximately 276 km/h, with a discrepancy of about 2% relative to the CEN (2025) formulation.
6. A simplified two-dimensional analytical beam model incorporating equivalent rotational stiffness at the beam ends is developed to represent the global dynamic behaviour of skew bridges. The analytical free-vibration analysis accurately predicts the first three flexural modes, with discrepancies within 1–1.4% compared with the three-dimensional finite element results. The resonance speed predicted by the analytical

approach is approximately 280 km/h, differing from the 3D FEM result by about 1.4%.

7. Increasing the skew angle leads to higher natural frequencies and a nonlinear increase in resonance speed, while the maximum displacement decreases nonlinearly and the maximum acceleration remains nearly unchanged.
8. Increasing the elastic modulus results in higher natural frequencies and critical speeds, reduced maximum displacement, and only minor variations in maximum acceleration.
9. A parametric investigation of fifteen cross-sectional configurations grouped into three categories provides the corresponding resonance speeds, maximum displacements, and maximum accelerations over a range of train speeds. These results can be used as a basis for selecting optimal cross-sectional geometries suitable for high-speed railway bridges.

REFERENCES

1. Fryba. Dynamics of Railway Bridges. Thomas Telford Ltd., London; 1996.
2. Eurocode – Basis of structural design. London: British Standards Institution (BSI); 2023. Report No.: BS EN 1990:2023.
3. European Committee for Standardization (CEN). EN 1991-2 (2023): Eurocode 1: Actions on structure - Part 2: Traffic loads on bridges. 2023.
4. Kollbrunner CF, Basler K. Torsion in Structures. Berlin, Heidelberg: Springer; 1969.
5. Ashebo DB, Chan THT, Yu L. Evaluation of dynamic loads on a skew box girder continuous bridge Part I: Field test and modal analysis. Eng Struct. 2007;29:1052–63. https://doi.org/10.1016/j.engstruct.2006.07.014
6. He XH, Sheng XW, Scanlon A, Linzell DG, Yu XD. Skewed concrete box girder bridge static and dynamic testing and analysis. Eng Struct. 2012;39:38–49. https://doi.org/10.1016/j.engstruct.2012.01.016
7. Menassa C, Mabsout M, Tarhini K, Frederick G. Influence of skew angle on reinforced concrete slab bridges. J Bridge Eng. 2007;12:205–14. https://doi.org/10.1061/(ASCE)1084-0702(2007)12:2(205)
8. Romo J, Perez-Caldentey A, Cuadrado M. High-speed Railway Bridges: Conceptual Design Guide. 1st ed. Berlin: Wiley; 2023.
9. Ministry of Transport and Sustainable Mobility. Informative study of the Elche railway arterial network: connection variant of the new high-speed rail station with the urban centre, Annex No. 7. Structures (in Spanish). Madrid, Spain; 2020. https://www.transportes.gob.es/ferrocarriles/estudios-en-tramite/elche-estacion-centro-urbano
10. Ministry of Transport and Sustainable Mobility. Informative study of the Cantabrian–Mediterranean high-speed rail corridor, Zaragoza–Castejón section, Annex No. 9. Structures (in Spanish). 2018. https://www.transportes.gob.es/ferrocarriles/estudios-en-tramite/estudios-y-proyectos-en-tramite/estudio-informativo-del-corredor-cantabrico-mediterraneo-de-alta-velocidad-tramo-zaragoza-castejon
11. Kaliyaperumal G, Imam B, Righiniotis T. Advanced dynamic finite element analysis of a skew steel railway bridge. Eng Struct. 2011;33:181–90. https://doi.org/10.1016/j.engstruct.2010.10.003
12. Chopra AK. Dynamics of Structures: Theory and Applications to Earthquake Engineering. 5th ed. Pearson; 2017.
13. Paz M. Structural Dynamics: Theory and Computation. 5th ed. Springer Science & Business Media; 2012.
14. Meng J-Y, Lui EM. refined stick model for dynamic analysis of skew highway bridges. J Bridge Eng. American Society of Civil Engineers; 2002;7:184–94. https://doi.org/10.1061/(ASCE)1084-0702(2002)7:3(184)
15. Meng JY, Lui EM, Liu Y. Dynamic response of skew highway bridges. J Earthq Eng. Taylor & Francis Group; 2001;5:205–23. https://doi.org/10.1080/13632460109350392
16. Yi Meng J, Lui EM. Seismic analysis and assessment of a skew highway bridge. Eng Struct. 2000;22:1433–52. https://doi.org/10.1016/S0141-0296(99)00097-8
17. Ashebo DB, Chan THT, Yu L. Evaluation of dynamic loads on a skew box girder continuous bridge Part II: Parametric study and dynamic load factor. Eng Struct. 2007;29:1064–73. https://doi.org/10.1016/j.engstruct.2006.07.013
18. Karnovsky IA, Lebed O. Formulas for Structural Dynamics: Tables, Graphs and Solutions. McGraw Hill Professional; 2000.
19. Maragakis EA, Jennings PC. Analytical models for the rigid body motions of skew bridges. Math Comput Model. 1989;12:377. https://doi.org/10.1016/0895-7177(89)90115-5
20. Nguyen K, Velarde C, Goicolea JM. Analytical and simplified models for dynamic analysis of short skew bridges under moving loads. Adv Struct Eng. 2019;22:2076–88. https://doi.org/10.1177/1369433219831481
21. Clough RW, Penzien J. Dynamics of Structures. 2nd ed. McGraw-Hill International Editions; 1993.
22. Ministry of Public Works. Instruction on actions to be considered in railway bridges (IAPF-07) (in Spanish). 2007.
23. Dassault Systèmes. Abaqus User's Manual, Version 2024. Dassault Systèmes Simulia Corp; 2024.